

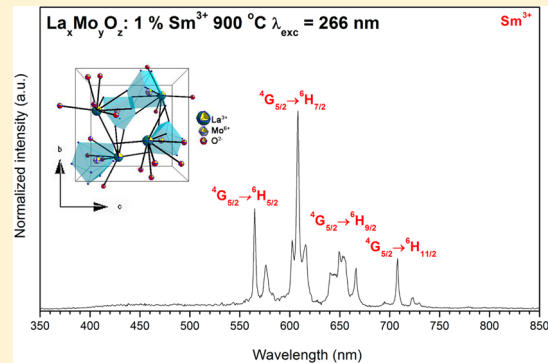
# Lanthanum Molybdate Nanoparticles from the Bradley Reaction: Factors Influencing Their Composition, Structure, and Functional Characteristics as Potential Matrixes for Luminescent Phosphors

Sarah Abtmeyer,<sup>†</sup> Robert Pązik,<sup>‡</sup> Rafał J. Wiglusz,<sup>‡</sup> Małgorzata Małecka,<sup>‡</sup> Gulaim A. Seisenbaeva,<sup>†</sup> and Vadim G. Kessler\*,<sup>†</sup>

<sup>†</sup>Department of Chemistry, Biocenter SLU, Box 7015, 75007 Uppsala, Sweden

<sup>‡</sup>Institute of Low Temperature and Structure Research, PAS, Okólna 2, 50-422 Wrocław, Poland

**ABSTRACT:** Interaction of lanthanum isopropoxide with molybdenum (VI) alkoxides in La/Mo ratios varying from 3:1 to 1:1 in acetophenon or allyl alcohol as solvents offers nanosized poorly crystalline products of complex composition, where the precipitation of Mo-rich ones is followed by the formation of La-rich ones with conservation of the reaction stoichiometry in total. Thermal treatment of the precipitates at temperatures over 700 °C leads to the formation of stoichiometric phases of the  $\alpha$ - and  $\beta$ -La<sub>2</sub>Mo<sub>2</sub>O<sub>9</sub> compositions. Introduction of smaller Re<sup>3+</sup> cations such as Sm<sup>3+</sup> by doping favors stabilization of the La<sub>2-x</sub>RE<sub>x</sub>Mo<sub>2</sub>O<sub>9</sub> phase with improved crystallinity even after lower-temperature thermal treatment. The doping is successful only when the Re<sup>3+</sup> (Sm<sup>3+</sup>, Eu<sup>3+</sup>, and Tb<sup>3+</sup>) is introduced as an alkoxide: application of Re<sup>3+</sup>(acac)<sub>3</sub> as Re<sup>3+</sup> sources leads to materials free from Re<sup>3+</sup>. The produced samples were characterized by XPD, TGA, SEM, and TEM studies as well as the luminescent properties for the Sm<sup>3+</sup>-doped phases.



## 1. INTRODUCTION

During recent years, rare-earth molybdates have attracted strong attention because of their important functional properties that range from their ionic conductivity<sup>1–4</sup> and catalytic activity for applications in solid-oxide fuel cells<sup>5</sup> to their superior light-absorption capacity in the UV-vis region, making them attractive for use as matrixes for RE-based luminescent phosphor materials.<sup>6–8</sup> The latter are especially attractive in the form of well-defined nanoparticles for bioimaging applications because of the potentially low toxicity of molybdenum and rare-earth cations.<sup>9</sup> Preparation of molybdates in the nano form is rather challenging because of the facile sintering of the particles. The traditional sol-gel<sup>10,11</sup> and Pechini<sup>7</sup> approaches commonly provide relatively large aggregates where the grains are strongly bound to each other. Hydrothermal synthesis with oleic acid and oleylamine as surfactants also produced relatively large 200 × 100 nm<sup>2</sup> tetragonal bipyramidal crystals of stoichiometric NaLa(MoO<sub>4</sub>)<sub>2</sub>.<sup>12</sup> In the absence of surfactants in the hydrothermal synthesis, an extensive aggregation was observed. The use of only oleic acid or only oleylamine was not successful in preventing the aggregation.

An attractive surfactant-free approach to small-size, uniform hydrophilic nanoparticles is the Bradley reaction,<sup>13–15</sup> which exploits the low-temperature decomposition of metal alkoxide or related O-donor ligand precursors via ether elimination in alcohol or a carbonyl compound (aldehyde or ketone) as solvent. In many cases, it has been demonstrated to offer

crystalline Perovskite nanoparticles directly from the wet chemical synthesis without subsequent thermal treatment.<sup>16</sup> In fact, the direct formation of crystalline metal-oxide nanoparticles in the Bradley reaction was first observed for alkaline and alkaline-earth molybdates.<sup>17,18</sup> Taking into account that lanthanum and molybdenum alkoxides have been revealed to be prone to form heterometallic complexes in solution,<sup>19</sup> it was plausible to expect facile formation of lanthanum molybdate nanoparticles by this approach.

In the present study, we intended to identify the conditions permitting the preparation of uniform size and crystalline lanthanum molybdate nanoparticles by the Bradley reaction and to investigate the possibility of doping them with other RE elements, in particular, Sm<sup>3+</sup>, for the preparation of nano-phosphors.

## 2. EXPERIMENTAL DETAILS

X-ray diffraction (XRD) patterns were collected in a 2θ range of 5–100° with an X'Pert Pro PANalytical X-ray diffractometer (Cu K $\alpha$  = 1.54060 Å) equipped with beam monochromator. Thermogravimetric analysis (TGA) was performed using Pyris 1 TGA combined with a PerkinElmer FTIR Spectrum 100 system. The microstructure and morphology of the La<sub>x</sub>Mo<sub>y</sub>O<sub>z</sub> nanoparticles were investigated by means of high-resolution transmission electron microscopy (HRTEM) using a Philips CM-20 Super Twin microscope operated at 200 kV.

**Received:** September 17, 2013

**Published:** January 6, 2014

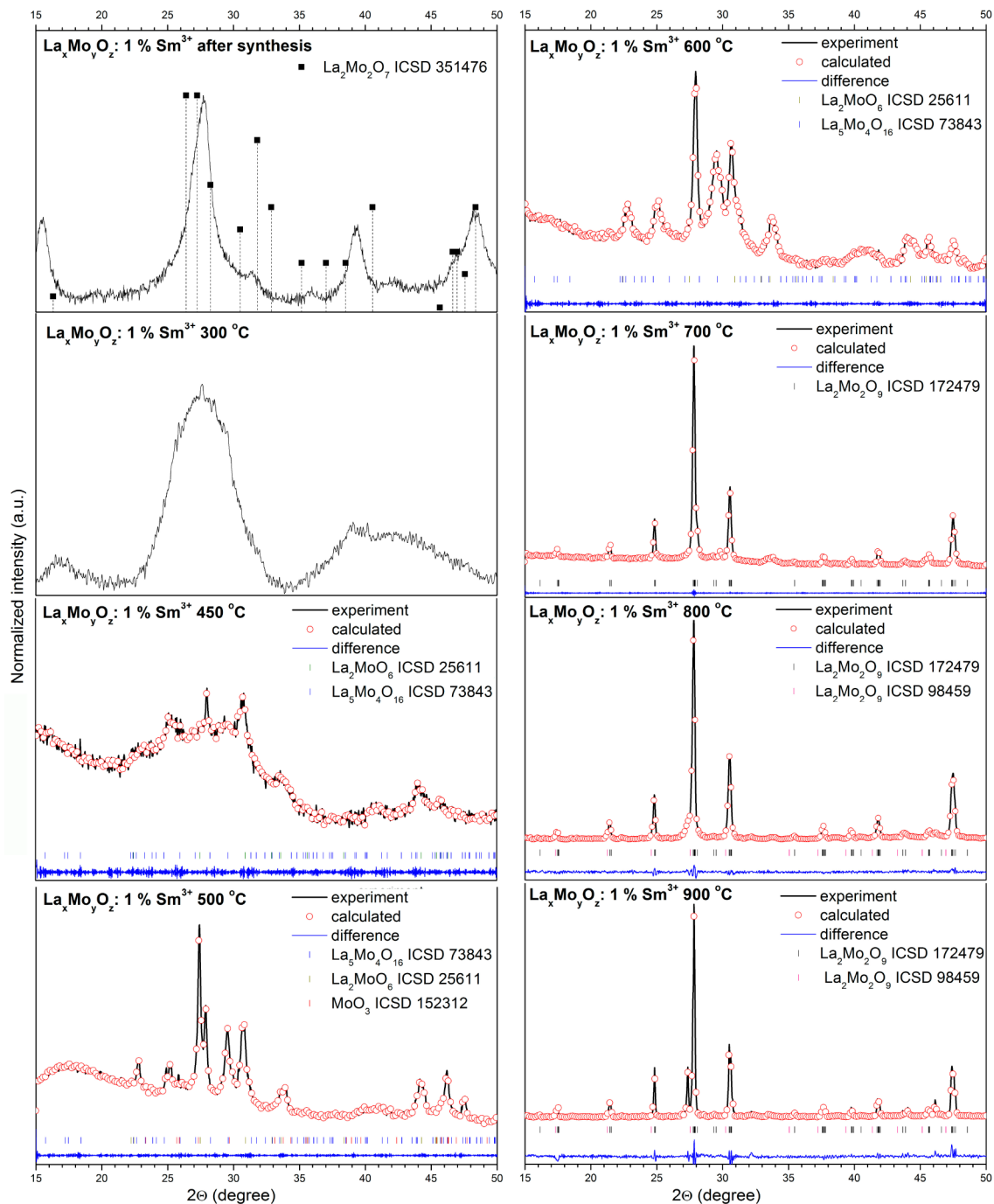


**Figure 1.** Temperature evolution of the  $\text{La}_2\text{Mo}_2\text{O}_9$  system. Black lines are the experimental patterns, red circles are the results of the Rietveld fitting, and blue lines are differential lines.

Samples for HRTEM measurements were prepared by dispersing the powders in methanol and depositing a droplet of the suspension on a copper microscope grid covered with perforated carbon. The luminescence measurements were performed on a Lincam THMS600 stage using the third harmonic of the YAG:Nd<sup>3+</sup> laser,  $\lambda_{\text{exc}} = 266 \text{ nm}$ , as an excitation source and a Hamamatsu PMA-12 as a detector. The detection setup exhibits a relatively flat response in the spectral range of interest.

**Synthesis of  $\text{La}_x\text{Mo}_y\text{O}_z:\text{Sm}^{3+}$  Powders.**  $\text{MoO}(\text{OMe})_4$  was obtained by anodic oxidation of molybdenum metal and was purified by recrystallization from hexane as described elsewhere.<sup>19</sup>  $\text{La}(\text{O}^{\prime}\text{Pr})_3$  and  $\text{Sm}(\text{O}^{\prime}\text{Pr})_3$  were purchased from Multivalent Laboratory and used without further purification. In a typical procedure applied for the synthesis of material, a mixture of lanthanum and molybdenum

alkoxides in a 1:1 molar ratio and total mass of about 0.5 g together with 0.01 or 0.02 equiv of  $\text{Sm}(\text{O}^{\prime}\text{Pr})_3$  was dissolved in 20 mL of dry acetophenone and subjected to reflux for 16 h. The resulting brown powder was separated by sedimentation overnight with subsequent decantation of the solvent, washed with three portions of 5 mL of ethanol, and dried in air.

### 3. RESULTS AND DISCUSSION

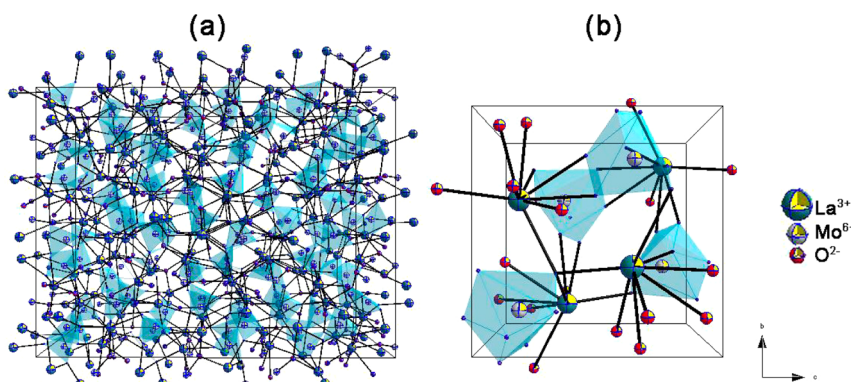
**3.1. Phase Analysis and Structure Evolution.** The structure evolution with temperature of the stoichiometric  $\text{La}_2\text{Mo}_2\text{O}_9$  system doped with 1 mol % of  $\text{Sm}^{3+}$  ions was followed by XRD measurements starting directly from powders, isolated and purified from the reaction mixture, on which

**Table 1.** Unit Cell Parameters ( $a$ ,  $b$ ,  $c$ , and  $\beta$ ), Crystal Cell Volume ( $V$ ), and Number of Phases as well as Refined Factor ( $R_{wp}$ ) for the  $\text{La}_5\text{Mo}_4\text{O}_{16}$ ,  $\text{La}_2\text{MoO}_6$ , and  $\text{MoO}_3$  Phases as a Function of the Sintering Temperature

sample <sup>a</sup>	cell parameters					phase			$R_{wp}$ (%)
	$\text{La}_5\text{Mo}_4\text{O}_{16}$ (1) <sup>24</sup>		$\text{La}_2\text{MoO}_6$ (2) <sup>2</sup>			(1)	(2)		
	$a$ (Å)	$b$ (Å)	$c$ (Å)	$\beta$	$V$ (Å <sup>3</sup> )	$a$ (Å)	$c$ (Å)	$V$ (Å <sup>3</sup> )	
s.c.	7.9638(7)	7.9958(5)	10.3345(7)	95.067(6)	655.5	4.089(0)	15.99(0)	267.35	
600 °C	9.8937(9)	8.9640(4)	10.4767(6)	95.190(5)	925.43	4.652(1)	17.720(4)	372.33	68.44
500 °C	8.4308(3)	8.1410(4)	10.4554(2)	98.805(0)	709.16	4.101(9)	15.995(3)	269.13	50.97
450 °C	8.3674(0)	8.2400(7)	10.8154(8)	98.540(1)	737.51	4.378(1)	16.271(5)	311.89	98.59
	$\text{MoO}_3$ (3) <sup>425</sup>					phase			
sample <sup>a</sup>	$a$ (Å)		$b$ (Å)	$c$ (Å)	$V$ (Å <sup>3</sup> )	(3)			
s.c.	3.9614(4)		13.8621(9)	3.6970(2)	203.01(3)				
500 °C	4.0670(0)		13.5952(2)	3.3451(5)	185.31				33.18

<sup>a</sup>s.c., single-crystal reference data.**Table 2.** Unit Cell Parameters ( $a$ ,  $b$ ,  $c$ , and  $\beta$ ) and Crystal Cell Volume ( $V$ ) as well as Refined Factor ( $R_{wp}$ ) for the  $\alpha$ - and  $\beta$ - $\text{La}_2\text{Mo}_2\text{O}_9$  Phases as a Function of the Sintering Temperature

sample <sup>a</sup>	cell parameters					phase			$R_{wp}$ (%)
	$\alpha\text{-La}_2\text{Mo}_2\text{O}_9$ (1) <sup>26</sup>		$\beta\text{-La}_2\text{Mo}_2\text{O}_9$ (2) <sup>27</sup>			(1)	(2)		
	$a$ (Å)	$b$ (Å)	$c$ (Å)	$\beta$	$V$ (Å <sup>3</sup> )	$a$ (Å)	$V$ (Å <sup>3</sup> )		
s. c.	14.325(3)	21.482(4)	28.585(6)	90.40(3)	8796.24	7.235(1)	378.73		
900 °C	14.312(4)	21.477(0)	28.619(0)	90.37(5)	8796.93	7.335(4)	394.70	98.35	1.65
800 °C	14.328(1)	21.466(3)	28.619(2)	90.33(1)	8802.30	7.235(1)	378.73	98.95	1.05
700 °C	14.305(6)	21.481(0)	28.644(3)	90.19(2)	8802.30			100.00	3.65

<sup>a</sup>s.c., single-crystal reference data.**Figure 2.** Projection of the unit cells of the  $\alpha$  (a) and  $\beta$  (b) modifications of  $\text{La}_2\text{Mo}_2\text{O}_9$  along the  $c$  axis.

additional annealing steps were then performed up to 900 °C (Figure 1). As can be seen, the temperature behavior of the samples on their way toward crystallization of the desired phase from the starting product derived from metal alkoxides was quite complex. It involved several processes including crystallization of the byproducts, their decomposition, formation of multiphase systems, and further recrystallization leading to the formation of the desired composition as well as a phase transition from  $\alpha$ - to the  $\beta\text{-La}_2\text{Mo}_2\text{O}_9$  structure. To obtain better insight into the transformations of the samples, phase analysis based on Rietveld refinement<sup>20</sup> using an anisotropic approach<sup>21,22</sup> with Maud 2.0 software<sup>23</sup> was done after each thermal-treatment step (Tables 1 and 2). Despite the well-developed diffraction lines, the accurate phase identification and Rietveld refinement of the after-synthesis sample was almost impossible because of the significantly broadened Bragg's reflections and overlapping of the peaks that are possibly related to other compositions containing La, Mo, and

O elements. Another factor complicating the identification of the initial phase was the presence of an amorphous fraction and of residual organic impurities. However, the best match could be made using a reference standard of the  $\text{La}_2\text{Mo}_2\text{O}_7$  phase containing a reduced form of molybdenum ( $\text{Mo}^{4+}$ ). Unfortunately, any attempt at structure refinement did not give satisfactory results and led to unacceptable error values. The width of the peaks indicates the presence of ultrasmall particles, but when they are exposed to a high-energy electron beam during TEM measurement, they start to recrystallize in real time, revealing the thermodynamic instability of the product and making this analysis extremely difficult.

This conclusion is further supported by the XRD pattern of the sample after annealing at 300 °C, where only the presence of the amorphous phase could be detected, which was manifested by the appearance of broad peaks with relatively low intensity. This clearly indicates that the after-synthesis material has started to decompose into an amorphous phase,

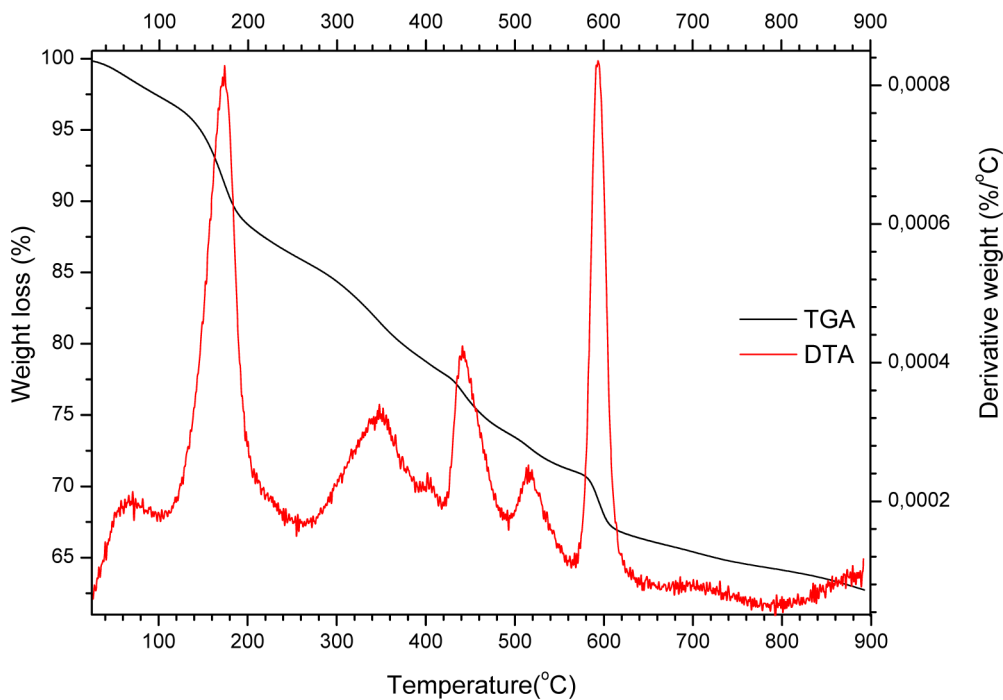


**Figure 3.** TGA analysis of the after-synthesis sample of  $\text{La}_x\text{Mo}_y\text{O}_z:\text{Sm}^{3+}$ .

which undergoes the next transformation into a more defined and crystalline product at temperatures over  $450\text{ }^{\circ}\text{C}$ .

Detailed structural analysis of that sample showed that the material consists of almost 98.6% of the  $\text{La}_5\text{Mo}_4\text{O}_{16}$  (mixture of the  $\text{Mo}^{4+}$  and  $\text{Mo}^{5+}$  oxidation states) phase and less than 2% of the  $\text{La}_2\text{MoO}_6$  (only  $\text{Mo}^{6+}$ ) phase. This confirms that under such reaction conditions during the Bradley process the  $\text{Mo}^{n+}$  ion becomes reduced, producing the  $\text{Mo}^{4+}$  ion. Further thermal treatment at  $500\text{ }^{\circ}\text{C}$  under an oxidative atmosphere leads to the oxidation of  $\text{Mo}^{4+}$  into  $\text{Mo}^{5+}$  ions or to a higher oxidation state because a drastic decrease in the amount of the  $\text{La}_5\text{Mo}_4\text{O}_{16}$  phase (around 60%) and an increase in the amount of the  $\text{La}_2\text{MoO}_6$  and  $\text{MoO}_3$  phases were observed. It could thus be concluded that the complete decomposition of the  $\text{La}_5\text{Mo}_4\text{O}_{16}$  phase (i.e., the oxidation of reduced forms of Mo) was completed at temperatures exceeding  $600\text{ }^{\circ}\text{C}$ . Finally, the phase mixture containing the above-mentioned compounds transforms into a pure  $\alpha\text{-La}_2\text{Mo}_2\text{O}_9$  phase at  $700\text{ }^{\circ}\text{C}$ . According to the structural analysis, no other secondary phases, impurities, or amorphous forms could be detected, thus confirming the formation of the designed compound. It should be underscored that  $\text{La}_2\text{Mo}_2\text{O}_9$  exhibits two different crystallographic polymorphs: a high-temperature cubic  $\beta$ -phase and a monoclinic one described in literature as a low-temperature modification, which could reversibly transform into  $\beta\text{-La}_2\text{Mo}_2\text{O}_9$  under heating the  $\alpha$ -phase to  $580\text{ }^{\circ}\text{C}$ .<sup>26</sup> It is necessary to describe here the  $\text{La}_2\text{Mo}_2\text{O}_9$  structures in order to introduce some important features (Figure 2).  $\beta\text{-La}_2\text{Mo}_2\text{O}_9$  is isostructural with the cubic  $\beta\text{-SnWO}_4$   $P2_13$ , so the arrangement of the metal cations is pretty much the same and the only difference lies in the arrangement of oxygen anions and in the oxygen stoichiometry. The structure consists of different polyhedra like  $\text{MoO}_4$ ,  $\text{MoO}_5$ ,  $\text{LaO}_7$ , and  $\text{LaO}_8$ . Moreover, the molybdenum polyhedra are separated from each other, and lanthanum polyhedra are connected together via oxygen ions.<sup>28</sup> The unit cell of  $\beta\text{-La}_2\text{Mo}_2\text{O}_9$  contains 32 atoms: 4 La, 4 Mo, and 24 O, where all La and all Mo atoms are represented by only one crystallo-

graphic position and only 3 different types of symmetrically independent oxygen atoms are present (O1, O2, and O3).

The related cubic structure of  $\beta\text{-SnWO}_4$  has two fully occupied oxygen sites: one on the 3-fold axis and one in a general position. In  $\beta\text{-La}_2\text{Mo}_2\text{O}_9$ , there exist three unique oxygen atoms: O1 on the 3-fold axis and two other in partially occupied sites (O2 in the equatorial plane of the cation perpendicular to the 3-fold axis and O3<sup>28</sup> with a lower occupancy). In the case of the  $\alpha\text{-La}_2\text{Mo}_2\text{O}_9$  (monoclinic  $P12_11$ ), the asymmetric unit cell contains 312 crystallographically independent atoms: 48 La, 48 Mo, and 216 O, making it one of the largest oxide structures with complexity comparable to a small protein. However, it should be noted that in this complex structure the La/Mo sites are dominating and individual M–O bond lengths are relatively large. This in turn leads to an uncertainty in individual bond valence sums of up to half of a unit.<sup>28</sup> In comparison to the  $\beta\text{-La}_2\text{Mo}_2\text{O}_9$  compound, La atoms are coordinated in a shell containing between 6 and 12 oxygen atoms with 30 out of 48 independent La atoms with 9-fold coordination. It has been shown earlier that the substitution of lanthanide ions like  $\text{Y}^{3+}$ ,  $\text{Sm}^{3+}$ ,  $\text{Gd}^{3+}$ , and  $\text{Er}^{3+}$  on the La<sup>3+</sup> site leads to the suppression of the  $\alpha \leftrightarrow \beta$  transition and can stabilize the  $\beta$ -phase at room temperature.<sup>29</sup> What can be seen from the last two steps of the thermal treatment at 800 and  $900\text{ }^{\circ}\text{C}$  is the increase in the content of the  $\beta$  modification up to 1.7%, which is probably connected with the presence of the Sm<sup>3+</sup> ions (around 1 mol %). The latter most likely have a stabilizing effect on  $\beta\text{-La}_2\text{Mo}_2\text{O}_9$ . This behavior was even more pronounced in the luminescence properties of the Sm<sup>3+</sup> (the optical properties of the prepared system are described in section 3.4).

**3.2. TGA and DTA Analysis.** Thermo-gravimetric analysis of powders purified from the reaction mixture was performed under air to identify the processes occurring during the thermal treatment (Figure 3). The first mass loss up to  $100\text{ }^{\circ}\text{C}$  was attributed to the desorption of remaining ethanol and possibly water present in the sample as a result of the purification steps.

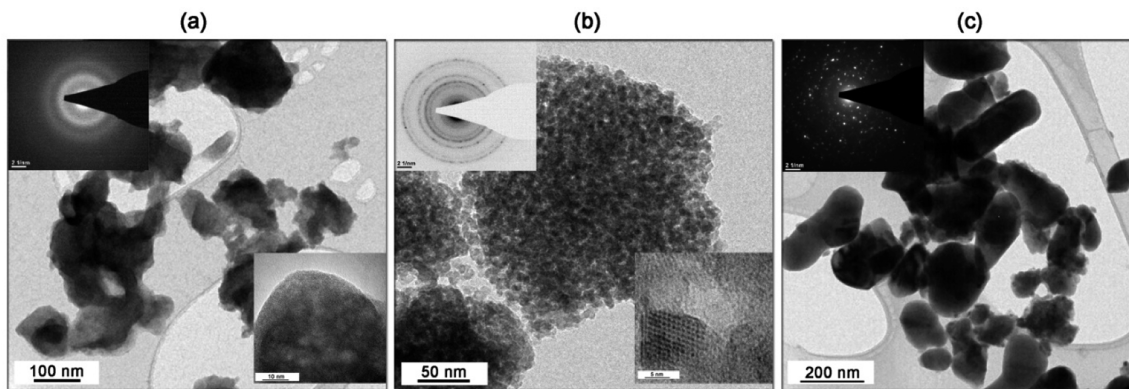


**Figure 4.** TEM and SAED images of the (a) after-synthesis sample of  $\text{La}_x\text{Mo}_y\text{O}_z:\text{Sm}^{3+}$ , (b)  $\text{La}_2\text{Mo}_2\text{O}_9:\text{Sm}^{3+}$  treated at  $700\text{ }^\circ\text{C}$ , and (c)  $\text{La}_2\text{Mo}_2\text{O}_9:\text{Sm}^{3+}$  annealed at  $900\text{ }^\circ\text{C}$ .

Next, the heating step led to a quite well-defined decomposition of the organic components occurring with maximal speed at  $140\text{--}160\text{ }^\circ\text{C}$  and completing when the temperature reached  $240\text{ }^\circ\text{C}$ . This is a typical temperature regime for the decomposition of residual alkoxide groups,<sup>30</sup> and the resulting product is a completely amorphous oxide.

This step is also usually associated with formation of residual graphitic carbon. The following step occurs between  $240\text{ }^\circ\text{C}$  and about  $400\text{ }^\circ\text{C}$ . It most likely corresponds to the combustion of the graphitic carbon on the surface of the oxide aggregates and the first transformation in their morphology associated with the partial crystallization of the reduced phases. The two following steps were then, in turn, associated with further structural transformation of the oxide material with deeper and deeper exposure and combustion of the residual carbon. The last sharply defined step in weight loss took place after  $580\text{ }^\circ\text{C}$  and finished at  $650\text{ }^\circ\text{C}$ . Under these conditions, the molybdenum cations were finally oxidized completely into  $\text{Mo}^{6+}$  centers, and the material turned fully crystalline and carbon-free. Further slow weight loss is associated with an apparent minor loss of  $\text{Mo}^{4+}$  in the form of the volatile  $\text{MoO}_3$  under these conditions, which can lead to a minor substoichiometry of the produced phases in relation to Mo.

**3.3. TEM and SAED Analysis.** To investigate the morphology and structure of the final products, TEM and SAED characterization were carried out for the after-synthesis sample as well as for the  $\text{La}_2\text{Mo}_2\text{O}_9:\text{Sm}^{3+}$  samples heat-treated at  $700$  and  $900\text{ }^\circ\text{C}$  (Figure 4). Because of the strong interaction of the high-energy electron beam with the after-synthesis sample, it was extremely difficult to find areas with direct evidence of any long-range order because of the quick decomposition process that resulted in the formation of a totally amorphous phase (as indicated in the XRD section). The product after electron irradiation contains fairly big objects with poorly defined shapes that form large agglomerates. The SAED image confirms the absence of any long-range order because the reflection rings were very broad and strongly diffused.

The particles of the  $\text{La}_2\text{Mo}_2\text{O}_9:\text{Sm}^{3+}$  heat-treated at  $700\text{ }^\circ\text{C}$  were uniform with regular shapes and tended to coalesce into agglomerates containing a large number of grains. It is worth noting that the single-particle size was relatively small (14 nm on average) but agglomerates were about 200 nm or larger in size. This appearance is indicative of random nucleation with limited growth, a phenomenon that is typical for a metal-

organic decomposition (MOD) process occurring as a solid-state reaction.<sup>30</sup> This construction facilitates the subsequent Ostwald ripening-type transformation upon further thermal treatment. In the case of the powder samples heated at  $900\text{ }^\circ\text{C}$ , the grain size increases significantly up to  $60\text{--}400\text{ nm}$ , yielding irregular and often elongated crystallites. The spotty SAED patterns in both cases confirm the crystallization of the precursor into the final products.

**3.4. Optical Properties in Connection with Structural Changes.** To shed light on the luminescence issues in the prepared samples, it is important to discuss first the general aspects of the  $\text{Sm}^{3+}$  ion spectroscopic properties. Usually, the emission spectrum of  $\text{Sm}^{3+}$  exhibits four distinct emission peaks corresponding to the transitions of  ${}^4\text{G}_{5/2} \rightarrow {}^6\text{H}_{5/2}$  at around 560 nm,  ${}^4\text{G}_{5/2} \rightarrow {}^6\text{H}_{7/2}$  at 595 nm,  ${}^4\text{G}_{5/2} \rightarrow {}^6\text{H}_{9/2}$  with a maximum at 640 nm, and  ${}^4\text{G}_{5/2} \rightarrow {}^6\text{H}_{11/2}$  at 700 nm. Furthermore, each of the bands is split because of the Stark effect of the  ${}^4\text{G}_{5/2}$  state. Of course, several other transitions could be observed both from the  ${}^4\text{G}_{5/2} \rightarrow {}^6\text{F}_J$  ( $J = 1/2$  to  $9/2$ ) as well as  ${}^6\text{H}_{13/2}$ ; however, their intensities were, in most cases, rather low with a maxima observed in the near IR spectral region (870–1150 nm).<sup>31</sup> Among the aforementioned  ${}^4\text{G}_{5/2} \rightarrow {}^6\text{H}_J$  transitions of  $\text{Sm}^{3+}$ , the first one ( ${}^4\text{G}_{5/2} \rightarrow {}^6\text{H}_{5/2}$ ) is a purely magnetic dipole transition, the second one ( ${}^4\text{G}_{5/2} \rightarrow {}^6\text{H}_{7/2}$ ) is a partly magnetic and partly forced electric dipole transition, and the third one ( ${}^4\text{G}_{5/2} \rightarrow {}^6\text{H}_{9/2}$ ) is a typical electric dipole transition.<sup>32</sup> Analogous to the  $\text{Eu}^{3+}$  ion, the electric dipole transition is extremely sensitive to even slight changes in the local environment of the  $\text{Sm}^{3+}$  ion. Generally, when the  $\text{Eu}^{3+}$  ions occupy the position with a center of symmetry, the only allowed transition is the magnetic dipole one, whereas in a noncentrosymmetric site, the electric dipole transition becomes very intense. The same logic could be adopted for the analysis of the  $\text{Sm}^{3+}$  behavior.<sup>33</sup> Therefore, the ratio between the intensities of the electric dipole  ${}^4\text{G}_{5/2} \rightarrow {}^6\text{H}_{9/2}$  transition to the partial magnetic dipole  ${}^4\text{G}_{5/2} \rightarrow {}^6\text{H}_{7/2}$  transition could be treated as an asymmetry parameter

$$R = \frac{I({}^4\text{G}_{5/2} \rightarrow {}^6\text{H}_{9/2})}{I({}^4\text{G}_{5/2} \rightarrow {}^6\text{H}_{7/2})}$$

and could be considered as indicative of the asymmetry of coordination polyhedron of the  $\text{Sm}^{3+}$  ion. Thus, the higher the ratio, the farther from a centrosymmetric geometry the  $\text{Sm}^{3+}$  is located.<sup>32</sup>

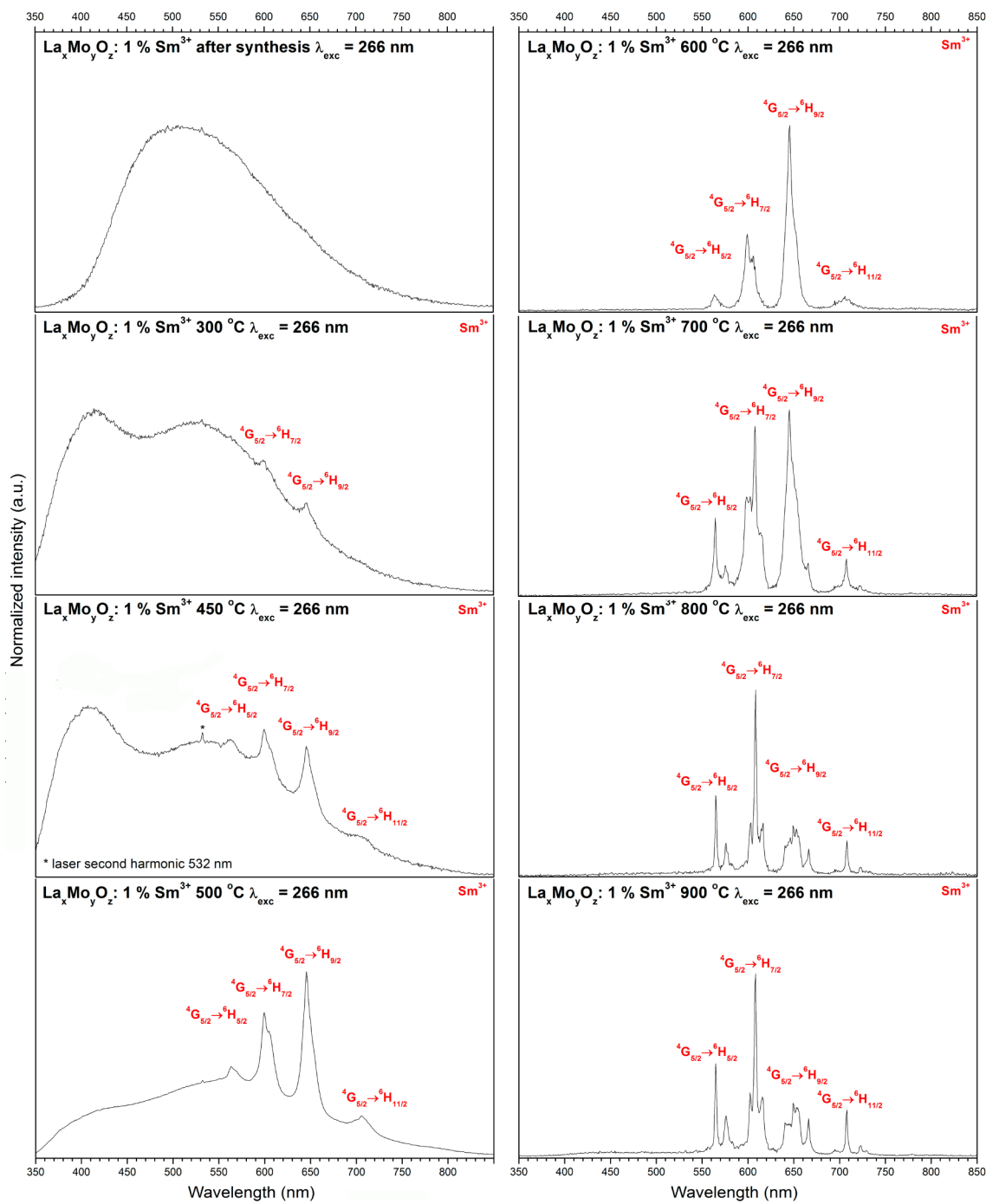


**Figure 5.** Variation of the emission spectra of the  $\text{La}_x\text{Mo}_y\text{O}_z:\text{Sm}^{3+}$  system as a function of the sintering conditions.

Figure 5 displays the variation of the emission spectra of the  $\text{La}_x\text{Mo}_y\text{O}_z:\text{Sm}^{3+}$  system, which directly follows the structural changes induced by the annealing conditions (cf. Figure 1). In the case of the powder denoted as the after-synthesis sample, the spectra did not contain any traces of the  $\text{Sm}^{3+}$  ions emission and revealed only a very broad band. As the temperature increased, it split into a double band at about  $500\text{ }^{\circ}\text{C}$ , and it vanished completely when the temperature exceeded  $600\text{ }^{\circ}\text{C}$ . The interpretation of the nature of these bands is quite complex because the system was apparently completely amorphous and of a complex composition at  $300\text{ }^{\circ}\text{C}$ . However, it is beyond any doubt that their appearance is due to the host lattice structural changes and is connected with the presence of complex

structures containing  $\text{Mo}^{n+}$  ions in different oxidation states ( $\text{Mo}^{4+}$ ,  $\text{Mo}^{5+}$ , and  $\text{Mo}^{6+}$ ), which in turn might lead to the formation of color centers, resulting in broad-band emission. Additionally, the changes in the color of the powders during the thermal treatment from light brown through dark gray and eventually to white above  $500\text{ }^{\circ}\text{C}$  support the existence of at least two different color centers. In fact, one of the methods for color-center removal is further temperature treatment, leading to an increase in the degree of crystallinity coupled with a decrease in the net and surface defects in the sample. Of course, one might imply the presence of charge-transfer (CT) emission of the type  $\text{O}^{2-} \rightarrow \text{Mo}^{(4+,5+,6+)}$ . However, the CT transitions are strongly prone to quenching in systems containing lanthanides

where there is a possibility of CT state relaxation to the excited states of the respective lanthanide ions because of the crossover between them (Figure 6). This phenomenon is common in the

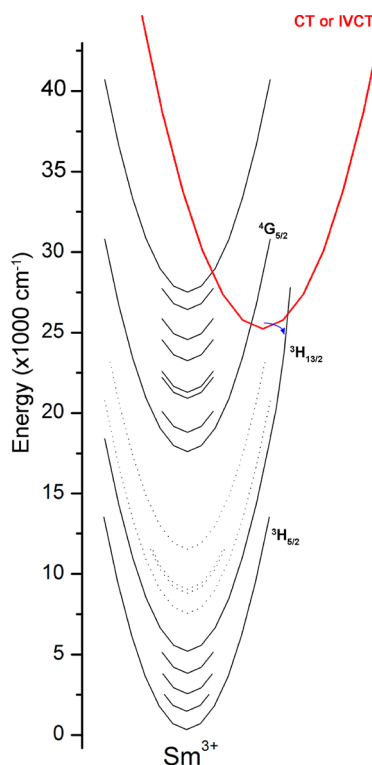


**Figure 6.** Simplified configurational coordinate diagram of  $\text{Sm}^{3+}$  illustrating possible routes for quenching of the CT or IVCT emissions.

host lattices containing  $\text{Eu}^{3+}$ ,  $\text{Tb}^{3+}$ , or  $\text{Sm}^{3+}$ .<sup>34</sup> Even for the exceptional case of  $\text{Yb}^{3+}$  where there is actually no crossover of the CT state with the  $^2\text{F}_{5/2}$  excited state of the  $\text{Yb}^{3+}$  because of the large energy difference, the CT band still could not be observed at room temperature because of the low thermal

activation energy of luminescence quenching. The mechanism of this quenching was fully described by the Struck–Fonger model where the origin of the CT transition involves not only charge delocalization between  $\text{O}^{2-}$  and lanthanide cation but also other types of CT transitions, for instance, like the intervalence charge-transfer transitions (IVCT) typical for oxide lattices containing closed-shell transition-metal groups (titanoates, vanadates, tungstates, and molybdates).<sup>35,36</sup> The S–F mechanism would involve the crossover of the CT or IVCT states with the parabola describing the ground state of the respective lanthanide. In addition to the described quenching because of crossover from the CT excited state to the ground state, the photoionization process should also be mentioned. The latter mechanism is particularly important in thermally activated luminescence quenching involving the escape of a hole from a charge-transfer state directly to the valence band and should be taken into consideration as well.

The  $\text{Sm}^{3+}$  emission apparently evolved together with the structure changes. In the case of the after-synthesis sample, the emission of  $\text{Sm}^{3+}$  was clearly completely quenched, most probably because of the fact that the most of the optically active ions were located close to the surface area and were susceptible to the interaction with the impurities or to the formation of  $\text{Sm}^{3+}$  ion pairs, leading to the nonradiative relaxations. The same could possibly be true for the amorphous sample treated at 300 °C, where only traces of  $\text{Sm}^{3+}$  emission could be detected. However, further increase of the annealing temperature led to the enhancement of the  $\text{Sm}^{3+}$  ions emission connected with the formation of crystalline phases. Nonetheless, the shape and broadening of the emission bands suggests luminescence behavior characteristic of a still rather amorphous material because the level of crystallinity of the particles was low at 450 °C. The situation changed drastically at 500 °C. All characteristic  $\text{Sm}^{3+}$  transitions could then be easily identified as a result of long-range order improvement and better crystallinity of the product composed of  $\text{MoO}_3$ ,  $\text{La}_5\text{Mo}_4\text{O}_{16}$ , and  $\text{La}_2\text{MoO}_6$  phases. Further thermal treatment at 600 °C, associated with the oxidation of  $\text{Mo}^{4+}$  and  $\text{Mo}^{5+}$  into  $\text{Mo}^{6+}$ , led to an increase in  $\text{La}_2\text{MoO}_6$  phase content and better  $\text{Sm}^{3+}$

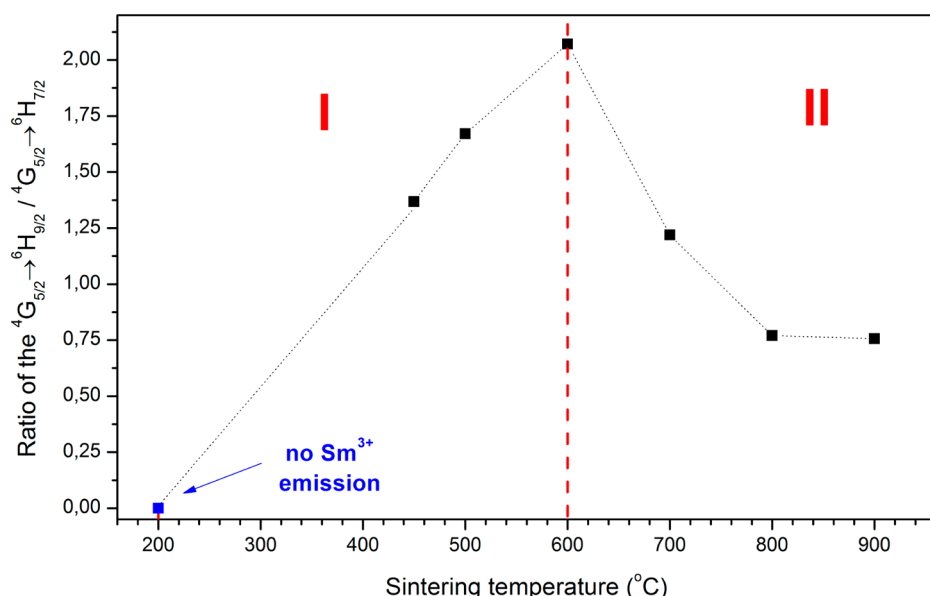


**Figure 7.** Temperature-induced asymmetry-ratio changes of  $^4\text{G}_{5/2} \rightarrow ^6\text{H}_{9/2}$  /  $^4\text{G}_{5/2} \rightarrow ^6\text{H}_{7/2}$  (dotted lines are provided as a guide to the eye).

emission intensity. The next step of annealing at 700 °C allowed for separation of several Stark components of Sm<sup>3+</sup> electron transitions because optically active ions occupied well-defined crystallographic sites upon formation of the pure  $\alpha$ -La<sub>2</sub>Mo<sub>2</sub>O<sub>9</sub> phase. Additionally, a decrease in the intensity of the  $^4G_{5/2} \rightarrow ^6H_{9/2}$  electric dipole transition was observed at the expense of the partial magnetic dipole  $^4G_{5/2} \rightarrow ^6H_{7/2}$  transition, pointing out the less deformed environment of this site occupied by Sm<sup>3+</sup> in comparison to the multiphase sample treated at 600 °C. As could be seen from the XRD patterns, the sample showed the coexistence of  $\alpha$  and  $\beta$  polymorphs, with decreasing content of the former above 700 °C. According to the crystal structure data available from the literature, the site symmetry of La<sup>3+</sup> in  $\alpha$ -La<sub>2</sub>Mo<sub>2</sub>O<sub>9</sub> is C<sub>2</sub>, whereas in  $\beta$ -La<sub>2</sub>Mo<sub>2</sub>O<sub>9</sub>, this position is in the higher *T* point symmetry. Such behavior was directly mirrored in the Sm<sup>3+</sup> luminescence behavior as well. First, the possible number of Stark components of each energy level was dependent on the quantum number of the total angular momentum, *J*, of the energy level and the number of electrons of the considered ion.<sup>37</sup> Thus, following Kramer's theorem,<sup>38</sup> each energy level, *i*, splits into a maximum number, *s<sub>i max</sub>* of Stark levels with  $(2J + 1)/2$  for an odd number of electrons at low symmetry. Hence, the number of Stark components for the  $^4G_{5/2} \rightarrow ^6H_{7/2}$  at C<sub>2</sub> symmetry should be equal four, whereas for *T* site symmetry, only a maximum three Stark levels should be observed in the spectra. This is exactly the case when one compares the difference relying on the domination of the electric dipole transition and the magnetic one in the spectra at 700 and 800 °C or 900 °C. Moreover, because at the C<sub>2</sub> site there is no symmetry inversion, the electric dipole transition  $^4G_{5/2} \rightarrow ^6H_{9/2}$  dominated the spectra. Upon  $\beta$ -phase stabilization at higher temperatures, it was evident that the most intense band is the magnetic dipole  $^4G_{5/2} \rightarrow ^6H_{7/2}$  transition, pointing out the changes of the closest surrounding of the Sm<sup>3+</sup> ions. The plot presenting the asymmetry parameter was divided into two main regions: one covering the range of temperatures where no Sm<sup>3+</sup> ions emission was detected because only amorphous or multiphase products were obtained (Figure 7) and a second that shows changes of the *R* parameter where all materials were characterized by a satisfactory crystallization level and the presence of well-defined phases. The values of the asymmetry parameter give more convincing results regarding the ordering and/or decrease of the distortion of the coordination polyhedron of the Sm<sup>3+</sup> ion and the site symmetry increase upon stabilization of the  $\beta$ -phase. The value of this parameter vastly decreased with the increase in the sintering temperature, showing that the Sm<sup>3+</sup> ions could be treated as a specific optical probe for detection of structural changes.

Additionally, the presence of the  $^4G_{5/2} \rightarrow ^6H_{9/2}$  transition above 800 °C and the higher number of Stark components than expected for *T* site might suggest that some of the Sm<sup>3+</sup> ions were still located in the low-symmetry sites as well. It has been reported that the complete stabilization of the high-temperature  $\beta$ -La<sub>2</sub>Mo<sub>2</sub>O<sub>9</sub> could be achieved only if the lanthanide content is higher than 25 mol %.<sup>39</sup> Although such a high dopant concentration is favorable in applications where high ionic conductivity materials are expected, in the context of optical materials, it is treated as a serious drawback because of the concentration quenching mechanism, leading to the non-luminescent materials. Control over the phase composition of the La<sub>2</sub>Mo<sub>2</sub>O<sub>9</sub> ( $\alpha \leftrightarrow \beta$ ) might be used in color tuning (yellow-orange) of the final phosphor by changing only the relative

ratio of the magnetic dipole transition versus the electric dipole one, which would be triggered by the annealing temperature.

## 4. CONCLUSIONS

A nonhydrolytic approach toward nanocrystalline La<sub>2</sub>Mo<sub>2</sub>O<sub>9</sub> powders doped with 1% Sm<sup>3+</sup> using simple metal-organic precursors as a source was proposed as an attractive route for fabrication of molybdate-based compounds. A detailed study of the precursors' transformation as a function of the applied temperature of a thermal treatment was performed to follow the structural changes of the intermediates and the formation of the desired La<sub>2</sub>Mo<sub>2</sub>O<sub>9</sub>:Sm<sup>3+</sup> compound. It was found that directly after synthesis the sample consisted of a mixture of amorphous oxide bearing residual organics together with very small crystalline particles that were most probably La<sub>2</sub>Mo<sub>2</sub>O<sub>7</sub>:Sm<sup>3+</sup> (containing reduced Mo<sup>4+</sup> ions), which could transform easily into the fully amorphous phase under electron-beam exposure. Additional annealing steps are quite complex and involve crystallization of the multiphase products with final formation of the La<sub>2</sub>Mo<sub>2</sub>O<sub>9</sub>:Sm<sup>3+</sup>. In the course of the studies, it was found that above 800 °C the stabilization of the high-temperature  $\beta$ -La<sub>2</sub>Mo<sub>2</sub>O<sub>9</sub>:Sm<sup>3+</sup> occurred, which was induced by the presence of heavier lanthanide ions and sintering temperature, leading to the coexistence of the  $\alpha$  and  $\beta$  phases. It was expected that a lanthanide ion concentration increase would lead to the complete stabilization of the  $\beta$ -type La<sub>2</sub>Mo<sub>2</sub>O<sub>9</sub>:Sm<sup>3+</sup>, even at room temperature. However, the balance between satisfactory luminescence properties and content of the Sm<sup>3+</sup> has to be found to ensure good emission behavior. It was shown that the nature of the broad-band emission for the samples heat-treated up to 500 °C was connected with the presence of multiphase systems containing Mo<sup>n+</sup> ions in different oxidation states (Mo<sup>4+</sup>, Mo<sup>5+</sup>, and Mo<sup>6+</sup>), which in turn led to the formation of color centers. Additionally, this was indirectly confirmed by the changes in the powder colors from light brown through dark gray and eventually to white above 500 °C. The broad-band emission vanishes with annealing temperature. The emission behavior of Sm<sup>3+</sup> (i.e., strong sensitivity of the electric dipole transition for subtle crystallographic changes) allows for detection of the structural changes of the respective host lattice. Furthermore, the control over the phase composition of La<sub>2</sub>Mo<sub>2</sub>O<sub>9</sub> ( $\alpha \leftrightarrow \beta$ ) might be used for color tuning (yellow–orange) of the final phosphor by changing only the relative ratio of the magnetic dipole transition versus the electric dipole one, which would be triggered by the annealing temperature.

## ■ AUTHOR INFORMATION

### Corresponding Author

\*E-mail: vadim.kessler@kemi.slu.se.

### Notes

The authors declare no competing financial interest.

## ■ ACKNOWLEDGMENTS

We thank Ewa Bukowska for performing the XRD measurements and Prof. Leszek Kępiński for access to the TEM instrumentation. The financial support of the National Science Centre for the project 'Smart Nanoparticles for Bioimaging and Drug Delivery' (no. UMO-2011/01/D/ST5/05827) is gratefully acknowledged. Support from the Swedish Research Council (Vetenskapsrådet) is also gratefully acknowledged.

## ■ REFERENCES

- (1) Corbel, G.; Lacorre, P. *J. Solid State Chem.* **2006**, *179*, 1339–1334.
- (2) Voronkova, V. I.; Kharitonova, E. P.; Orlova, E. I.; Kolesnikova, D. S. *Crystallogr. Rep.* **2011**, *56*, 1066–1069.
- (3) Hutchinson, T. P.; Radosavljević Evans, I. *Solid State Ionics* **2008**, *178*, 1660–1662.
- (4) Kharton, V. V.; Marques, F. M. B.; Atkinson, A. *Solid State Ionics* **2004**, *174*, 135–149.
- (5) Jacquens, J.; Farrusseng, D.; Georges, S.; Viricelle, J.-P.; Gaudillère, C.; Corbel, G.; Lacorre, P. *Fuel Cells* **2010**, *10*, 433–439.
- (6) Chen, Y. C.; Chen, T. M. *J. Rare Earths* **2011**, *29*, 723–726.
- (7) Pang, M. L.; Liu, X. M.; Lin, J. *J. Mater. Res.* **2005**, *20*, 2676–2681.
- (8) He, X. H.; Guan, M. Y.; Zhang, C. Y.; Shang, T. M.; Lian, N.; Zhou, Q. *F. J. Mater. Res.* **2011**, *26*, 2379–2383.
- (9) Bouzigues, C.; Gacoin, T.; Alexandrou, A. *ACS Nano* **2011**, *5*, 8488–8505.
- (10) Hou, Z. Y.; Chai, R. T.; Zhang, M. L.; Zhang, C. M.; Chong, P.; Xu, Z. H.; Li, G. G.; Lin, J. *Langmuir* **2009**, *25*, 12340–12348.
- (11) Li, H. Y.; Zhang, S. Y.; Zhou, S. H.; Cao, X. Q.; Zheng, Y. H. *J. Phys. Chem. C* **2009**, *113*, 13115–13120.
- (12) Bu, W. B.; Chen, Z. X.; Chen, F.; Shi, J. L. *J. Phys. Chem. C* **2009**, *113*, 12176–12185.
- (13) Bradley, D. C.; Chakravarti, B. N.; Wardlaw, W. J. *J. Chem. Soc.* **1956**, 4439–4442.
- (14) Yanovskaya, M. I.; Turevskaya, E. P.; Kessler, V. G.; Obvintseva, I. E.; Turova, N. Y. *Integr. Ferroelectr.* **1992**, *1*, 343–352.
- (15) Pažik, R.; Piasecka, E.; Malecka, M.; Kessler, V. G.; Idzikowski, B.; Śniadecki, Z.; Wiglusz, R. J. *RSC Adv.* **2013**, *3*, 12230–12243.
- (16) Pazik, R.; Tekoriute, R.; Häkansson, S.; Wiglusz, R.; Strek, W.; Seisenbaeva, G. A.; Gun'ko, Y. K.; Kessler, V. G. *Chem.—Eur. J.* **2009**, *15*, 6820–6826.
- (17) Turova, N. Y.; Kessler, V. G.; Kuchekko, S. I. *Polyhedron* **1991**, *10*, 2617–2628.
- (18) Kessler, V. G.; Turova, N. Y.; Panov, A. N.; Starikova, Z. A.; Yanovsky, A. I.; Struchkov, Y. T.; Benlian, D. *Polyhedron* **1998**, *17*, 4189–4193.
- (19) Kessler, V. G.; Turova, N. Y.; Panov, A. N.; Yanovsky, A. I.; Pisarevsky, A. P.; Struchkov, Y. T. *Polyhedron* **1996**, *15*, 335–338.
- (20) Rietveld, H. M. *J. Appl. Crystallogr.* **1969**, *2*, 65–71.
- (21) Delhez, R.; de Keijser, T. H.; Langford, J. I.; Louér, D.; Mittemeijer, E. J.; Sonneveld, E. J. In *The Rietveld Method*; Young, R. A., Ed.; Oxford University Press: Oxford, UK, 1993; pp 132–166.
- (22) Luterotti, L.; Scardi, P. *J. Appl. Crystallogr.* **1990**, *23*, 246–252.
- (23) Lutterotti, L.; Matthies, S.; Wenk, H.-R. *IUCrJ* **1999**, *21*, 14–15.
- (24) Leligny, H.; Ledesert, M.; Labbé, Ph.; Raveau, B.; McCarroll, W. H. *J. Solid State Chem.* **1993**, *105*, 143–150.
- (25) Leisegang, T.; Levin, A. A.; Walter, J.; Meyer, D. C. *Cryst. Res. Technol.* **2005**, *40*, 95–105.
- (26) Evans, I. R.; Howard, J. A. K.; Evans, J. S. O. *Chem. Mater.* **2005**, *17*, 4074–4077.
- (27) Georges, S.; Goutenoire, F.; Altorfer, F.; Sheptyakov, D.; Fauth, F.; Suard, E.; Lacorre, P. *Solid State Ionics* **2003**, *161*, 231–241.
- (28) Hou, C. J.; Zhang, X.; Liu, C.-S.; Wang, X. P.; Fang, Q. F. *Chin. Phys. Lett.* **2008**, *25*, 3342–3345.
- (29) Jin, T. Y.; Madhava Rao, M. V.; Cheng, C. L.; Tsai, D. S.; Hung, M. H. *Solid State Ionics* **2007**, *178*, 367–374.
- (30) Seisenbaeva, G. A.; Sundberg, M.; Nygren, M.; Dubrovinsky, L.; Kessler, V. G. *Mater. Chem. Phys.* **2004**, *87*, 142–148.
- (31) Bunzli, J. C. G.; Eliseeva, S. V. In *Lanthanide Luminescence: Photophysical, Analytical and Biological Aspects*; Hanninen, P., Harma, H., Eds.; Springer-Verlag, Berlin, 2011.
- (32) Reisfeld, R.; Panczer, G.; Patra, A.; Gaft, M. *Mater. Lett.* **1999**, *38*, 413–417.
- (33) Bünzli, J. C. G.; Choppin, G. R. *Lanthanide Probes in Life Chemical, and Earth Sciences: Theory and Practice*; Elsevier, Amsterdam, The Netherlands, 1979; Chapter 35.
- (34) van Pieterson, L.; Heeroma, M.; de Heer, E.; Meijerink, A. J. *Lumin.* **2000**, *91*, 177–193.
- (35) Fonger, W. H.; Struck, C. W. *J. Phys. Chem.* **1970**, *52*, 6364–6372.
- (36) Boutinaud, P.; Bettinelli, M.; Diaz, F. *Opt. Mater.* **2010**, *32*, 1659–1663.
- (37) Dieke, G. H.; Crosswhite, H. M. *Appl. Opt.* **1963**, *2*, 675–686.
- (38) Kramers, H. A. *Proc. R. Acad. Sci. Amsterdam* **1930**, *33*, 959.
- (39) Marrero-Lopez, D.; Nunez, P.; Abril, M.; Lavin, V.; Rodriguez-Mendoza, U. R.; Rodriguez, V. D. *J. Non-Cryst. Solids* **2004**, *345*–346, 377–381.